



Contents lists available at ScienceDirect

## Journal of Alloys and Compounds

journal homepage: <http://www.elsevier.com/locate/jalcom>Improvement of the magnetic properties of SrFe<sub>12</sub>O<sub>19</sub> ceramics by tailored sintering with SiO<sub>2</sub> additionJ.C. Guzmán-Mínguez<sup>a</sup>, L.M. Vicente-Arche<sup>a, b</sup>, C. Granados-Mirallas<sup>a</sup>, J.F. Fernández<sup>a</sup>, A. Quesada<sup>a, \*</sup><sup>a</sup> Instituto de Cerámica y Vidrio (CSIC), Kelsen 5, 28049, Madrid, Spain<sup>b</sup> Unité Mixte de Physique, CNRS, Thales, Université Paris-Saclay, Avenue Augustin Fresnel 1, 91767, Palaiseau, France

## ARTICLE INFO

## Article history:

Received 8 July 2020

Received in revised form

6 November 2020

Accepted 7 November 2020

Available online xxx

## Keywords:

Permanent magnets

Strontium ferrite

Grain growth inhibition

Sintering

## ABSTRACT

In order to obtain competitive strontium ferrite sintered magnets, SiO<sub>2</sub> and CaO are added to avoid exaggerated grain growth. Besides favoring proper densification, these additives prevent the collapse of coercivity associated to grain growth. However, these additives may lead to slight decreases in density and the formation of paramagnetic  $\alpha$ -Fe<sub>2</sub>O<sub>3</sub> that hampers magnetization. Here, with the motivation of simplifying the production process, we present a study to maximize the magnetic performance of strontium ferrite ceramics using silica as the sole additive. A microscopic study offers insights into the grain growth mechanism activated by Silica. As a result, a compromise between relative density, coercivity and saturation magnetization is attained. It is found that sintering for 4 h up to 1200 °C with a SiO<sub>2</sub> content of 1 wt% leads to the best compromise between coercivity, magnetization and density values. Competitive densities are reported in the absence of CaO, the usual co-additive. In addition, Confocal Raman Microscopy is employed for the first time to characterize the decomposition of strontium ferrite onto  $\alpha$ -Fe<sub>2</sub>O<sub>3</sub>.

© 2020 Elsevier B.V. All rights reserved.

## 1. Introduction

The development of rare-earth-free permanent magnets has been fueled in recent years by the criticality of rare-earths [1–3]. Out of the different alternatives to rare-earth magnets, hexaferrites present important advantages in terms of availability, price, resistance to corrosion and the environmental friendliness of their production [4,5]. Strontium ferrite (SrM), with a chemical formula SrFe<sub>12</sub>O<sub>19</sub> and the hexagonal magnetoplumbite structure [6], is the most common hexaferrite compound found in the permanent magnet market [7]. As a ferrimagnetic material, it presents a moderate saturation magnetization which is tightly bound to its hexagonal c-axis owing to its substantial uniaxial anisotropy [8,9].

The performance of a magnet is measured by its energy product (a figure of merit of the energy stored inside a magnetic volume), which increases with both the remanent magnetization and the coercivity [10]. In order to maximize the energy product of SrM ceramic magnets, a high density must be achieved while retaining

significant coercivity and remanence. The coercivity of a magnet depends on both intrinsic parameters (such as the magneto-crystalline anisotropy) and extrinsic ones, such as grain sizes and shapes [11]. In SrM, grain sizes around 1 μm lead to the highest coercivity, as coherent spin rotation is needed to reverse magnetization [9,12]. On the other hand, domain wall propagation, a rotation mechanism that leads to significantly reduced coercivities, is favored by larger grain sizes [13]. As a consequence, obtaining large energy products in SrM was initially a challenge, due to the fact that the sintering temperatures required for optimum densification lead to massive grain growth and a collapse of coercivity.

SiO<sub>2</sub> performs as an extremely effective grain growth inhibitor in SrM ceramics [14–16]. Unfortunately, the density of ceramic pellets slightly decreases with SiO<sub>2</sub> content, which is of great importance as the energy product of a magnet scales with the square of the density. In order to improve density while assuring grain size control, CaO is used as co-additive [17,18]. In addition, for SiO<sub>2</sub> contents above 1 wt%, SrM is known to partially decompose into  $\alpha$ -Fe<sub>2</sub>O<sub>3</sub> [14], which is paramagnetic at room-temperature (RT) [19], negatively affecting magnetization. Thus, in order to maximize the energy product, an optimum trade-off between density, coercivity and magnetization has to be reached by tuning sintering

\* Corresponding author.

E-mail address: [a.quesada@icv.csic.es](mailto:a.quesada@icv.csic.es) (A. Quesada).

temperature and SiO<sub>2</sub> content.

The mechanism by which SiO<sub>2</sub> inhibits grain growth, called reaction induced grain growth impediment, was postulated by Kools et al. [16], although very scarce works have further studied the topic. In particular, the question remains if enough density can be achieved without any additive other than SiO<sub>2</sub>.

In this work, we fine tune the optimum trade-off between additive content and sintering schedule that maximizes coercivity, magnetization and density in SrM ceramics by employing exclusively SiO<sub>2</sub> as additive, which would simplify the production process. Scanning electron microscopy (SEM) and vibrating sample magnetometer (VSM) analyses are employed to follow the grain growth inhibition and the influence of the sintering parameters and composition on the magnetic properties. In addition, the formation of the secondary  $\alpha$ -Fe<sub>2</sub>O<sub>3</sub> phase is characterized by X-ray diffraction (XRD) and Confocal Raman Microscopy (CRM), which is brought forward here as an appropriate tool to monitor and locate the formation and orientation of Fe<sub>2</sub>O<sub>3</sub> grains inside the SrM matrix.

## 2. Methods

The raw materials used in this study are commercial strontium ferrite powders (SrFe<sub>12</sub>O<sub>19</sub>, 99%), from Max Baermann GmbH (Germany) and Cab-O-Sil (nanoparticles of SiO<sub>2</sub> of 25 nm diameter, 99.99%). All the characteristics of the starting SrM material are presented in the Supplemental Information. The ferrite samples were prepared by incorporating different amounts of SiO<sub>2</sub>, i.e. 0.5, 1, 1.5 and 2 wt% to the SrFe<sub>12</sub>O<sub>19</sub> powders. The mixtures were fabricated by means of a low energy, dry mixing method, in order to not modify the characteristics of the ceramic powders. In particular, the dry dispersion process [20] allows to produce SrFe<sub>12</sub>O<sub>19</sub>/SiO<sub>2</sub> mixtures by using a 60 cm<sup>3</sup> nylon container for 5 min at 50 rpm using a tubular-type mixer (Mixer/Mill, 8000D SPEX Sample Prep., USA). The pressing of the precursor powders in 1 cm diameter cylindrical pellet shapes was performed in a uniaxial press (Press Tonindustrie, SEGER, Bremen-Germany) applying 250 MPa. Afterwards, the densification (sintering) of the samples was carried out in a conventional oven in air atmosphere, with heating and cooling rates of 5 °C per min. The temperatures reached were 1200 °C and 1300 °C and the dwell time 4 h. The density of the ceramics was measured by the Archimedes method, and using 5.1 g/cm<sup>3</sup> as the theoretical density value of SrM [4].

The characterization of the particle size and morphology was performed using secondary electron images of field emission scanning electron microscopy, FE-SEM (Hitachi S-4700) and a scanning electron microscope (TM-1000) with an acceleration voltage set at 15 kV. Compositional analysis was performed by X-ray diffraction (XRD, Siemens D5000, Munich, Germany, Cu K $\alpha$  radiation). Average grain size was determined from image analysis of the SEM micrographs. Besides, a homemade vibrating sample magnetometer (VSM) [21], whose maximum magnetic field is 1.3T, was used to characterize the magnetic properties of the sintered pellets at room-temperature (RT). It is important to point out that given that the maximum field applied by our VSM is 1.3 T, the magnetization values given here do not correspond to fully saturated SrM samples. For this reason, magnetization at 1.3T ( $M_{1.3T}$ ) is given instead of saturation magnetization ( $M_S$ ). The error in the magnetization value of our VSM is estimated at 6–8%.

The pellets were further characterized by confocal Raman microscopy (CRM) (Witec Alpha 300RA, Witec, Ulm, Germany). Raman spectra were obtained using a 532 nm excitation laser (green laser of Nd:YAG). The spectral resolution of the system is 0.02 cm<sup>-1</sup>, under the best measurement conditions. The Raman mappings measurements at RT were performed using a 100 $\times$  objective lens with a numerical aperture (NA) of 0.95. Collected

spectra, taking 30 points per line and 30 lines per image (900 spectra), were analyzed by using Witec Control Plus Software.

## 3. Results and discussion

First, we study the densification of pure phase SrM pellets, without SiO<sub>2</sub> additive. Fig. 1a shows a SEM micrograph of the starting powder. It shows a bimodal grain size distribution, with large particles with an average size  $D = 1.26 \mu\text{m}$ , and smaller particles with average size  $D = 0.2 \mu\text{m}$ . Fig. 1b corresponds to the dilatometry graph of the starting powder. In it, we observe that shrinkage starts at around 1000 °C. The maximum shrinkage rate at 1210 °C and at 1300 °C, densification is completed.

The densification and coercivity ( $H_c$ ) of the pure SrM ceramics were studied at 5 different sintering temperatures for 4 h. As the onset for exaggerated grain growth is known to be between 1200 °C and 1300 °C and the shrinkage rate maxima at 1210 °C, below 1200 °C exaggerated grain is much less probable. This fact is in agreement with the work by Hussain et al. [18] where a larger dwell time of 10 h at 1175 °C was studied as well to get a better densification profile. We compare this profile with longer dwell time to the 4 h sintering at 1200 °C. Table 1 summarizes the findings. We indeed observe a marked decrease of  $H_c$  at the temperatures at which densification starts to be significant, i.e. at 1175 °C 10 h and 1200 °C 4 h, and directly a collapse at 1300 °C reaching 164 Oe.

To avoid this drastic fall in the value of coercive, different percentages of the additive SiO<sub>2</sub> (0.5-1-1.5-2 wt %) have been added and the sintering performed at the temperatures that lead to relative densities above 90%, i.e.  $\geq 1175$  °C (the dwell time at 1175 °C was kept as 10 h, meanwhile the dwell time for the rest of temperatures was maintained at 4 h).

Fig. 2 shows SEM micrographs of the different samples treated to several temperatures with different contents of SiO<sub>2</sub>. Fig. 2a, d and 2g belong to samples treated at 1175 °C for 10 h, at 1200 °C and 1300 °C during 4 h, respectively, without SiO<sub>2</sub> addition. In them, it is appreciated how at those temperatures the formation of sintering necks and the coarsening of the particles begins. At 1300 °C, temperature at which the third stage of sintering starts, the presence of exaggerated elongated grains with rectangular shape is noticeable, indicating the onset of exaggerated grain growth. Those rectangular grains have lateral sizes in the range 100–1000  $\mu\text{m}$  (see SEM image in Fig. S2 of the Supplemental Information).

At 1175 °C and 1200 °C and without silica, Fig. 2a–d, grains with relatively straight grain boundaries can be observed. By adding 1 wt % of SiO<sub>2</sub>, at 1300 °C (Fig. 2h) grain growth is inhibited as there is no trace of exaggerated grains; while at 1175 and 1200 °C (Fig. 2b–e), faceted grains with much straighter grain boundaries are observed. The average grain size with the silica addition  $\geq 1$  wt% is reduced for the different temperature profiles in comparison with pure SrM samples (Table 1) and the microstructure is homogeneous across all samples. The fact that the microstructure shows more straight and defined grain boundaries indicates that a much reduced mass transport has taken place at grain boundaries compared to the samples without silica. It is worth to mention that an effective exaggerated grain growth inhibition occurs for the silica-modified SrM samples for all the temperature profiles.

This microstructural result is observed for the different silica additions and provides evidence that the reaction induced grain growth impediment mechanism postulated by Kools et al. [14] is indeed responsible for the grain growth inhibition [4,16]. Silica nanoparticles are a reactive additive with a low solid solution in SrM. Silica dissolves in SrM high chemical potential sites at a slow rate. Kools et al. state that a non-equilibrium gradient in free energy is created that generates a force opposing the grain boundary

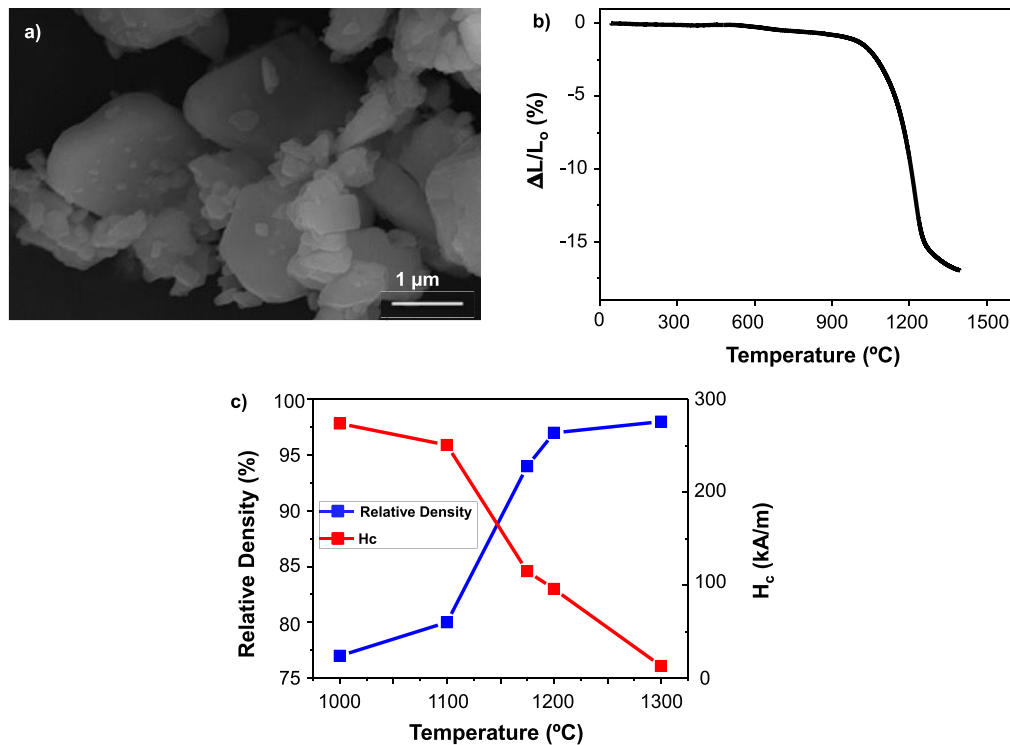


Fig. 1. a) FE-SEM micrograph of the starting powder, b) Dilatometry graph of the starting powder, c) Evolution of relative density and  $H_c$  for different sintering treatments.

Table 1

The table shows the coercive field ( $H_c$ ), saturation magnetization ( $M_{1.3T}$ ), average grain size ( $D$ ) and relative density values for each weight percentage of  $\text{SiO}_2$  added in each thermal treatment and commercial magnet (Y-35) from Supermagnet Company.

Sintering	$\text{SiO}_2$ (%wt)	$H_c$ (kA/m)	$M_{1.3T}$ (Am <sup>2</sup> /Kg)	$D$ (μm)	Relative Density (%)
1175°C-10h	0%	115	51	4.3	95
	0.5%	119	50	3.2	93
	1%	153	50	2.3	94
	1.5%	159	44	2.0	93
	2%	160	42	2.0	93
	0%	96	55	6.8	97
1200°C-4h	0.5%	104	55	4.7	94
	1%	136	54	3.6	96
	1.5%	139	45	3.8	96
	2%	144	44	3.8	94
	0%	13	58	68.4	98
	0.5%	32	57	34.7	96
1300°C-4h	1%	89	56	5.3	97
	1.5%	139	53	5.1	96
	2%	159	49	4.6	96
	—	177	59	—	95
Y-35	—	200	58	—	—
Starting Powder	0%	200	58	—	—

motion associated with grain growth. In fact, this gradient-generated force does not need to displace grain boundaries, and can therefore lead to completely stopped grain growth. The reactive phase is small in volume and homogeneously distributes along the grain boundaries, minimizing mass transport is minimized and equilibrating grain boundaries [22]. Our observations experimentally support this predicted consequence of the reaction induced mechanism, as grains of the order of 1–2 μm, sizes very close to those of the larger particles of the starting powders particles, can be observed in Fig. 2b–e. If we increase the additive content to 2 wt% (Fig. 2c, f and 2i) the grain inhibition effect is reproduced, although it is not straightforward to conclude if it has been accentuated with

respect to the lower silica contents. The dry dispersion process [20] leads to a homogeneous dispersion of the silica nanoparticles resulting in an effective exaggerated grain growth inhibition all across the samples.

The average grain size ( $D$ ) was measured from the SEM images for all samples studied. These values of  $D$ , together with the values of magnetization, coercivity and relative density for each sample are collected in Table 1.

As expected, average grain size decreases while coercivity increases with the amount of additive (see Fig. 3b). Silica addition limits grain size to average values half the ones of the pure SrM for the thermal treatments where no exaggerated growth takes place.

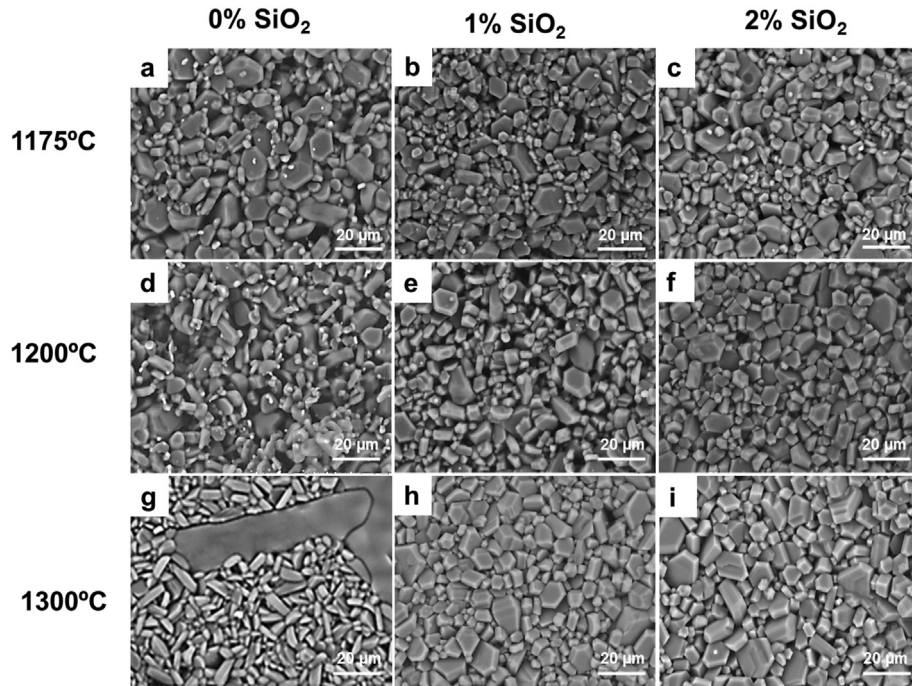


Fig. 2. FE-SEM micrographs of unpolished SrM ceramics with 0, 1 and 2 wt% of  $\text{SiO}_2$  sintered at 1175 °C, 1200 °C and 1300 °C.

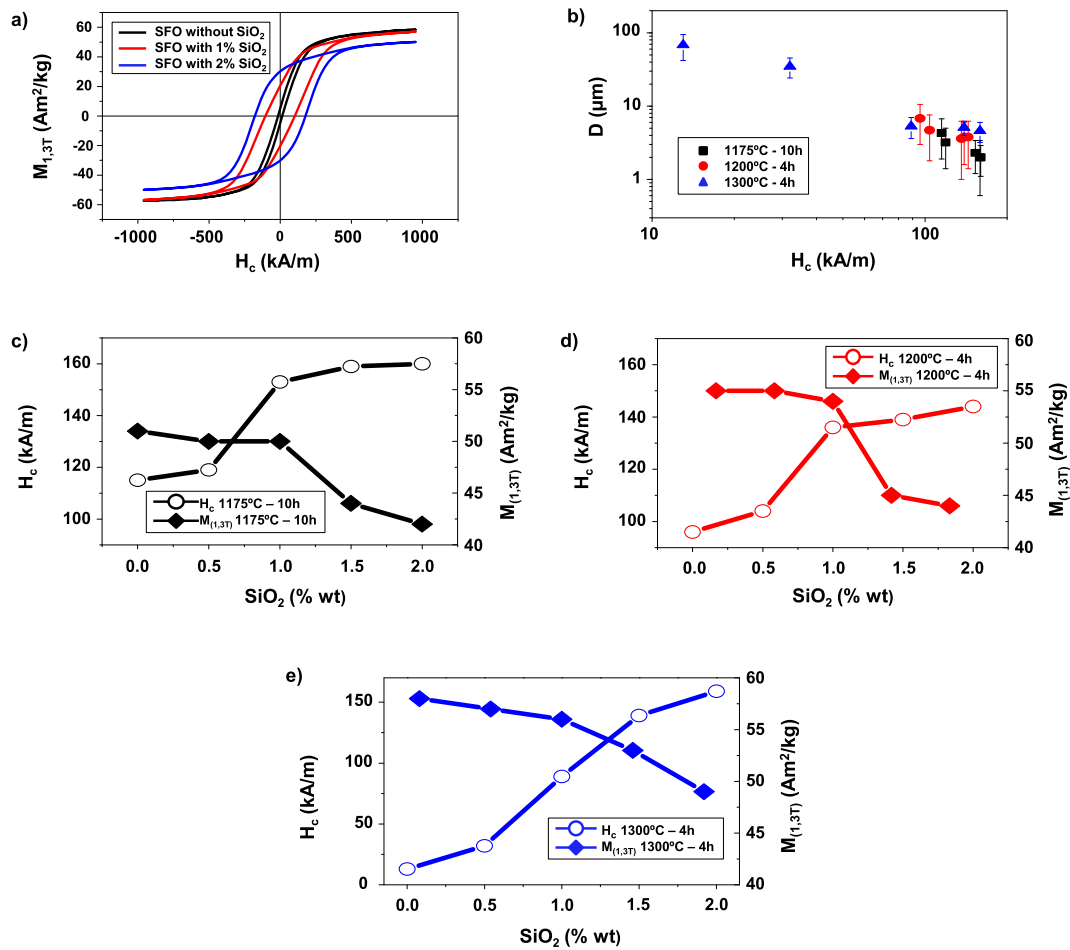


Fig. 3. a) Magnetization curves at RT of the pure SrM, 1 wt% and 2 wt%  $\text{SiO}_2$ , sintered at 1300 °C for 4 h. b) Relationship between average grain size and coercive field values for different sintered ferrites. Evolution of  $H_c$  and  $M_{1,3T}$  as a function of additive content for the c) 1175 °C 10 h, d) 1200 °C 4 h and e) 1300 °C 4 h sintered samples.



When the exaggerated grain occurs, at 1300 °C, the addition prevents such effect and the microstructure keeps its homogeneous appearance with limited grain growth. This occurs for silica additions  $\geq 1$  wt%. It is also worth mentioning that the SiO<sub>2</sub> contents explored reduce slightly the relative density when compared to the theoretical density of pure ferrites. This slight decrease of up to 2% in theoretical density is less pronounced for the higher silica contents. It is important to point out that even if this seems a negligible change, density has a very strong impact on the energy product of a magnet [2].

According to the values of the magnetic properties that appear in Table 1 and Fig. 3c–d, for the samples sintered at 1175 °C and 1200 °C, the addition of  $\geq 1$  wt% SiO<sub>2</sub> improves  $H_c$  by >33% in both cases, in agreement with the average grain decreasing. The effect in the samples sintered at 1300 °C/4h is much clearer (Fig. 3e), as the abnormal grain growth in the pure SrM sample collapses  $H_c$ . Silica addition  $\geq 1$  wt% leads to an average  $D = 5.3$   $\mu\text{m}$  and  $H_c = 2000$  Oe for samples densified  $\geq 96\%$  of the SrM theoretical density. Fig. 3a shows the magnetization curves of the samples at 1300 °C with different wt% of SiO<sub>2</sub>, clearly showing this drastic effect. Fig. 3b graphically shows the correlation between grain size and coercivity in a logarithmic scale: Coercivity clearly decreases as grain size increases. This detrimental effect of grain size in coercivity is well known [4,16]. It is due to the absence of pinning centers in large grains for magnetic domain walls that facilitates magnetization reversal and lowers  $H_c$ .

Contrary to coercivity, saturation magnetization drops with the amount of SiO<sub>2</sub>, with the maximum decrease representing a  $\sim 16\%$  with respect to the pure SrM. This fact is consistent with the partial decomposition of SrM onto Fe<sub>2</sub>O<sub>3</sub> upon addition of SiO<sub>2</sub> [16]. For 1 wt% SiO<sub>2</sub>, the  $M_{1,3T}$  decrease is <3% for 1200 °C. In Fig. 3c, d and 3e, this non-linear drop of  $M_{1,3T}$  with the SiO<sub>2</sub> content can be clearly observed. We estimate the error in the VSM measurement of the magnetization to be approximately  $\pm 10\%$  [20].

In order to further characterize the presence and microstructural arrangement of hematite in the SrM ceramics, CRM has been used. Results corresponding to the samples sintered at 1200 °C and 1300 °C and containing 1 and 2 wt% of SiO<sub>2</sub> are shown in Fig. 4.

Already in the optical images corresponding to 2 wt% SiO<sub>2</sub> sintered at 1200 °C and 1300 °C 4h (Fig. 4b and c), brighter grains having different morphological features are observed to be distributed in the SrM grain matrix. These brighter grains are absent in the samples with 1 wt% SiO<sub>2</sub> sintered at 1200 °C 4h. Each Raman image is a representation of the spectral mapping in which each pixel corresponds to a single Raman spectrum. For the sake of clarity, Raman spectra are identified by a color code. A correlation between the different microstructural regions is portrayed in the optical images, where the different colors correspond to the different phases. The ceramic matrix is identified as SrFe<sub>12</sub>O<sub>19</sub> (blue signaling in Raman images and the main Raman spectrum in Fig. 4d). The Raman spectrum of the SrFe<sub>12</sub>O<sub>19</sub>, has 5 main modes that are Raman-active:  $3A_{1g}$ ,  $1E_{1g}$  and  $1E_{2g}$ . The most intense  $A_{1g}$  mode is located at a Raman shift of 680  $\text{cm}^{-1}$  [23]. The assignments of the different Raman modes are indicated in Fig. 4d. In addition, two Raman modes assigned to SiO<sub>2</sub> are observed: one at 343  $\text{cm}^{-1}$  corresponding to the O–Si–O bending modes or torsional vibrations and other at 473  $\text{cm}^{-1}$  belonging to motions of O in Si–O–Si symmetric stretching–bending modes, indicated by asterisks in Fig. 4d [24].

The brighter grains of the optical images 4b and 4c present different Raman spectra, as evidenced in the red and green curves in Fig. 4d. Their Raman modes correspond to the spectrum of hematite [25,26], confirming that these irregular grains are indeed the secondary phase  $\alpha$ -Fe<sub>2</sub>O<sub>3</sub>. In both Raman spectra the same Raman modes are observed, which indicates that they both correspond to

hematite, although the Raman intensity differs. In one case (red Raman spectra), the  $A_{1g}$  mode at 244  $\text{cm}^{-1}$  is the most intense, whereas in the other (green Raman spectra) it is the  $E_g$  at 412  $\text{cm}^{-1}$ . We interpret these intensity differences as different crystallographic orientations of the hematite grains [27].

Each optical image, Fig. 4a, b and 4c, shows a correlated Raman image that presents in blue the ceramic regions with a large intensity of the 680  $\text{cm}^{-1}$  SrM mode, and in green/red the grains where the 415/244  $\text{cm}^{-1}$  hematite Raman modes are most intense. It is clear that for 1 wt% Silica, only the SrM matrix is detected. Higher amount of silica is associated with Raman images that show the presence of the isolated hematite grains (with the two crystallographic orientations) inside the SrM ceramic matrix. Identical experiments were performed for 1 and 2 wt% SiO<sub>2</sub> and all sintering temperatures. Grains of  $\alpha$ -Fe<sub>2</sub>O<sub>3</sub> were not observed in the Raman images maps for contents of 1 wt%, in agreement with the mild decays in  $M_{1,3T}$  observed in those samples. In fact, no trace of hematite was found either in the average spectra of the 1 wt% SiO<sub>2</sub>, as shown in Fig. 5a for each thermal treatment.

On the other hand, in Fig. 5b where the average Raman spectra of the 2 wt% SiO<sub>2</sub> ceramics are shown, the 244  $\text{cm}^{-1}$  hematite Raman mode can be clearly observed at temperatures  $\geq 1200$  °C. Interestingly, at 1175 °C hematite is not detected. This is consistent with the fact that, as mentioned before, the reaction of silica with SrFe<sub>12</sub>O<sub>19</sub> proceeds very slowly, for 2 wt% initially dissolving the ferrite matrix. The appearance of  $\alpha$ -Fe<sub>2</sub>O<sub>3</sub> occurs because the Sr<sup>2+</sup> cations are incorporated into the silica composition at grain boundaries due their glass network character, whereas the solid solution limit of Fe<sup>3+</sup> is more limited [16]. Ferrite ceramics sintered at 1175 °C for 10 h does not produce the segregation of hematite even for high SiO<sub>2</sub> contents. This is due to the slow rate of the dissolving reaction at 1175 °C [14]. This seems to indicate a correlation between the appearance of hematite and the maximum shrinkage rate.

XRD was employed to quantitatively estimate hematite formation in the 2 wt% SiO<sub>2</sub> sintered samples. Fig. 6 shows the XRD pattern of the sample sintered at 1200 °C 4 h with 2 wt% of SiO<sub>2</sub>. In the sample without SiO<sub>2</sub>, not shown, no secondary phases are observed. Rietveld analysis of the XRD data collected for the 2% silica modified ferrite yields a composition of 79(3) wt% of SrFe<sub>12</sub>O<sub>19</sub> (SrM) and 21(1) wt% of  $\alpha$ -Fe<sub>2</sub>O<sub>3</sub> (hematite). This is a surprisingly large amount of hematite considering previous works. It is likely that the absence of CaO as additive and the Sr/Fe ratio of the starting powder explain this observation. Given that hematite is paramagnetic at RT, this result is consistent with the 16% decrease in  $M_{1,3T}$  shown in Fig. 3, given the VSM experimental error. The unindexed peaks on the 2% SiO<sub>2</sub> data may correspond to this additive, but this phase was not considered in the Rietveld model, as such a low concentration is in the order of the detection limit of the experimental conditions.

By correlating all the experiments presented here, particularly the interplay between magnetization and coercivity in Fig. 3c, d and 3e, and the magnetic measurements of the commercial magnet that can be seen in Fig. S3 of the Supplemental Information, it is clear that the most competitive magnetic properties and densities are obtained for the sample containing 1 wt% SiO<sub>2</sub> and sintered at 1200 °C for 4 h. Grain growth control is quite effective for this silica addition, as only an extra 6% in  $H_c$  is gained by increasing it to 2 wt% SiO<sub>2</sub>. The relative density of the ceramic is 96%, a very competitive value considering that CaO was not used as an additive in this work. Saturation magnetization is practically the same as for the pure sample, given the experimental error. It is also clear that SiO<sub>2</sub> levels above 1.5 wt% need to be avoided as the decomposition to hematite is massively triggered, with a significant effect on  $M_{1,3T}$ . The sample sintered at 1300 °C and with a 1.5 wt% of SiO<sub>2</sub> presents the second

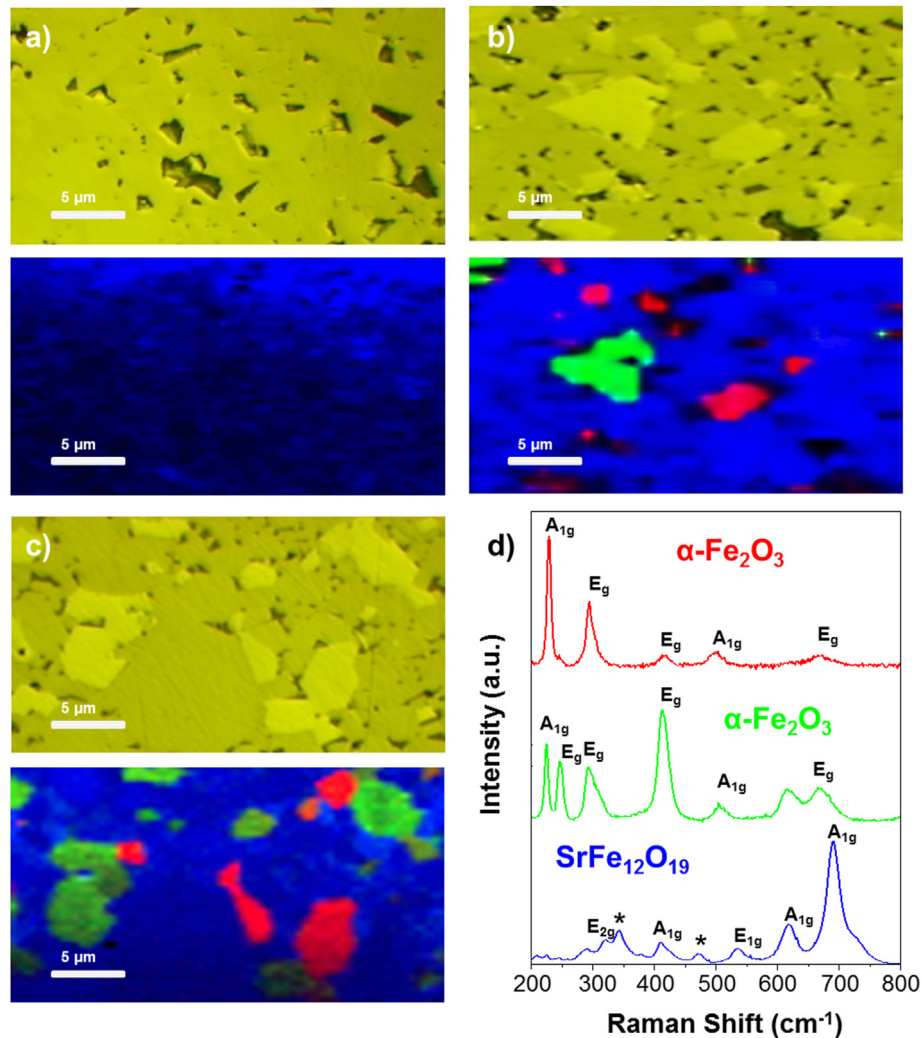


**Fig. 4.** Optical images (above) and Raman images (below) of SrM ceramics with a) 1 wt% SiO<sub>2</sub> sintered at 1200 °C 4h, b) 2 wt% SiO<sub>2</sub> sintered at 1200 °C 4h, c) 2 wt% SiO<sub>2</sub> sintered at 1300 °C 4h d) Average Raman spectra of each phase signaled by their corresponding color as:  $\alpha$ -Fe<sub>2</sub>O<sub>3</sub> (red and green color denoting two different crystallographic orientations) and SrFe<sub>12</sub>O<sub>19</sub> (blue). Raman mode assignment is denoted in each Raman spectrum. The Raman peak assigned by \* corresponds to Raman modes of SiO<sub>2</sub>. (For interpretation of the references to color in this figure legend, the reader is referred to the Web version of this article.)

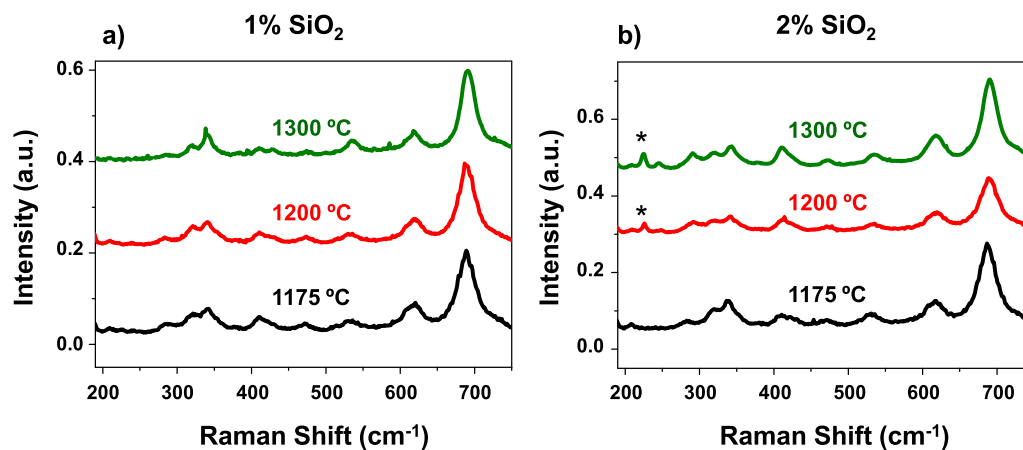


**Fig. 5.** a) Average Raman spectra for 1 wt% SiO<sub>2</sub> ceramics sintered at different temperatures. b) Average Raman spectra of samples with 2 wt% SiO<sub>2</sub> for each thermal treatment.

best compromise between the relevant properties.

In order to compare our optimized conditions with state of the art ferrite magnets, we present in Fig. 7 the demagnetization curves

of a magnetically oriented 1% silica SrM pellet sintered at 1200 °C for 4 h and a commercial ferrite magnet that has an energy product  $BH_{\max} = 32 \text{ kJ/m}^3$ , according to its specifications.

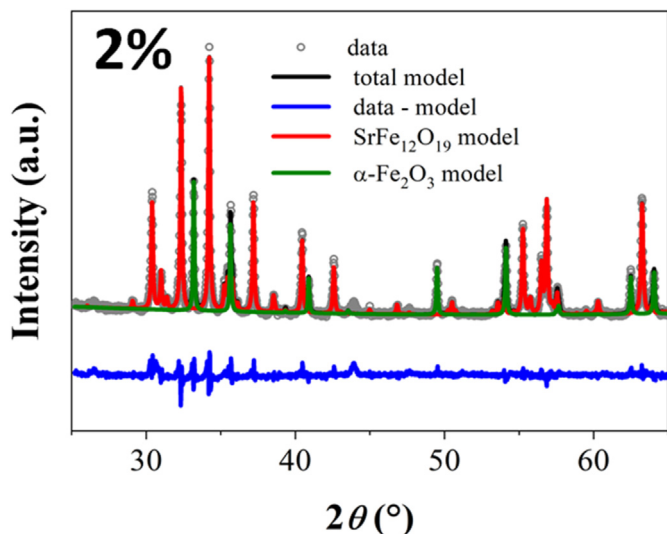


Fig. 6. XRD patterns of the 0%, 1% and 2% SiO<sub>2</sub> pellets sintered at 1200 °C for 4 h.

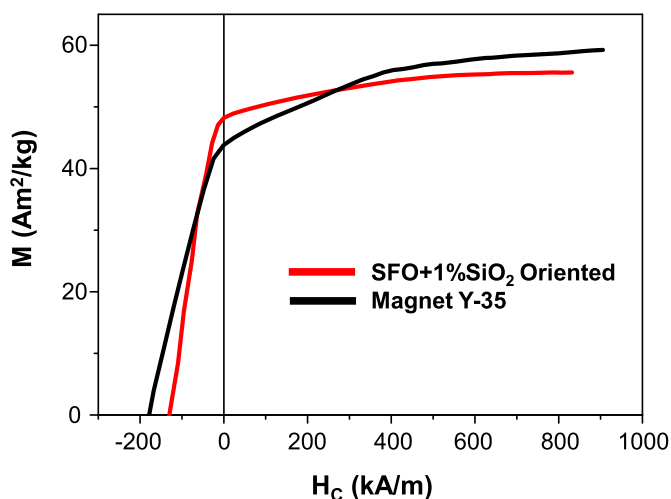


Fig. 7. Demagnetization curves up to 1.3 T of the magnetically oriented SrM pellet with 1% SiO<sub>2</sub> sintered at 1200 °C for 4 h (red) and a commercial magnet of grade Y-35. (For interpretation of the references to color in this figure legend, the reader is referred to the Web version of this article.)

As already presented and discussed in Table 1, our magnet presents slightly lower  $M_S$  and  $H_C$ . However, the remanence ( $M_R$ ) and  $M_R/M_S$  ratio is slightly higher; demonstrating that our procedure leads to competitive values overall and a good degree of magnetic texture.

#### 4. Conclusions

The grain growth inhibition process and the influence of silica content and sintering parameters on the grain size, magnetic properties and relative density of strontium ferrite ceramics have been studied. SiO<sub>2</sub> is confirmed to effectively suppress exaggerated grain growth and reduce grain growth, which strongly enhances the coercivity of the ceramic dense samples. Experimental evidence for the reaction induced mechanism that controls grain growth has been provided. For SiO<sub>2</sub> contents >1 wt%, the decomposition of SrM onto hematite significantly advances, reaching 21 wt% of secondary phase. By optimizing the sintering schedule, relative densities

above 95% are achieved by simply using SiO<sub>2</sub> as the sole additive, in the absence of the commonly used CaO co-additive. The best compromise between relative density, saturation magnetization and coercivity is obtained for an additive content of 1 wt% and a sintering schedule of 1200 °C for 4 h, which leads to SrM magnets with competitive magnetic properties compared to a state-of-the-art ferrite magnet. In addition, Raman microscopy is brought forward for the first time as a powerful tool to detect the presence and microstructural features of the secondary hematite phase that forms in this system. In a topic lead by magnet manufacturers in the last years, our work presents a concrete simplified strategy towards maximizing the magnetic performance of strontium ferrite magnets.

#### CRediT authorship contribution statement

**J.C. Guzmán-Mínguez:** Investigation, Writing - original draft, preparation. **L.M. Vicente-Arche:** Investigation. **C. Granados-Miralles:** Formal analysis, Data analysis. **J.F. Fernández:** Validation, Supervision, Conceptualization. **A. Quesada:** Conceptualization, Writing - review & editing, Supervision.

#### Declaration of competing interest

The authors declare that they have no known competing financial interests or personal relationships that could have appeared to influence the work reported in this paper.

#### Acknowledgements

This work is supported by the Spanish Ministerio de Ciencia, Innovación y Universidades through Project no. MAT2017-86450-C4-1-R, RTI2018-095303-A-C52 and through the Ramón y Cajal Contract RYC-2017-23320 and Juan de la Cierva Program FJC2018-035532-I; and by the European Commission through the H2020 Project no. 720853 (AMPHIBIAN).

#### Appendix A. Supplementary data

Supplementary data to this article can be found online at <https://doi.org/10.1016/j.jallcom.2020.157890>.

#### References

- [1] O. Gutfleisch, M.A. Willard, E. Brück, C.H. Chen, S.G. Sankar, J.P. Liu, Magnetic materials and devices for the 21st century: stronger, lighter, and more energy efficient, *Adv. Mater.* 23 (2011) 821–842, <https://doi.org/10.1002/adma.201002180>.
- [2] R.W. McCallum, L. Lewis, R. Skomski, M.J. Kramer, I.E. Anderson, Practical aspects of modern and future permanent magnets, *Annu. Rev. Mater. Res.* 44 (2014) 451–477, <https://doi.org/10.1146/annurev-matsci-070813-113457>.
- [3] D. Sander, S.O. Valenzuela, D. Makarov, C.H. Marrows, E.E. Fullerton, P. Fischer, J. McCord, P. Vavassori, S. Mangin, P. Pirro, B. Hillebrands, A.D. Kent, T. Jungwirth, O. Gutfleisch, C.G. Kim, A. Berger, The 2017 magnetism roadmap, *J. Phys. D Appl. Phys.* 50 (36) (2017), <https://doi.org/10.1088/1361-6463/aa81a1>.
- [4] R.C. Pullar, Hexagonal ferrites: a review of the synthesis, properties and applications of hexaferrite ceramics, *Prog. Mater. Sci.* 57 (2012) 1191–1334, <https://doi.org/10.1016/j.pmatsci.2012.04.001>.
- [5] A. Quesada, C. Granados-Miralles, A. López-Ortega, S. Erokhin, E. Lottini, J. Pedrosa, A. Bollero, A.M. Aragón, F. Rubio-Marcos, M. Stingaciu, G. Bertoni, C. de Julián Fernández, C. Sangregorio, J.F. Fernández, D. Berkov, M. Christensen, Energy product enhancement in imperfectly exchange-coupled nanocomposite magnets, *Adv. Electron. Mater.* 2 (2016), 1500365, <https://doi.org/10.1002/aeml.201500365>.
- [6] G.D. Soria, P. Jenus, J.F. Marco, A. Mandziak, M. Sanchez-Arenillas, F. Moutinho, J.E. Prieto, J. Cerdá, C. Tejera-Centeno, S. Gallego, M. Foerster, L. Aballe, M. Valvidares, H.B. Vasili, E. Pereiro, A. Quesada, J. de la Figuera, Strontium hexaferrite platelets: a comprehensive soft X-ray absorption and Mössbauer spectroscopy study, *Sci. Rep.* 9 (2019), <https://doi.org/10.1038/s41598-019-48010-w>.

- [7] G.V. Research, Permanent magnets market size, share & trends analysis report by material (ferrite, neodymium iron boron, aluminum nickel cobalt), by application (industrial, energy), by region, and segment forecasts, 2020 - 2027, 2020.
- [8] R. Skomski, J.M.D. Coey, Magnetic anisotropy - how much is enough for a permanent magnet? *Scripta Mater.* 112 (2016) 3–8, <https://doi.org/10.1016/j.scriptamat.2015.09.021>.
- [9] J.C. Faloh-Gandarilla, S. Díaz-Castañón, B.E. Watts, Magnetization reversal and interactions in SrFe<sub>12</sub>O<sub>19</sub>, *Phys. Status Solidi Basic Res.* 254 (2017) 1–7, <https://doi.org/10.1002/pssb.201600393>.
- [10] L.H. Lewis, F. Jiménez-Villacorta, Perspectives on permanent magnetic materials for energy conversion and power generation, *Metall. Mater. Trans.* 44 (2012) 2–20, <https://doi.org/10.1007/s11661-012-1278-2>.
- [11] M. Getzlaff, *Fundamentals of Magnetism*, M. Getzlaff, Pdf, Springer, Berlin, Heidelberg, 2007, <https://doi.org/10.1007/978-3-540-31152-2>.
- [12] A.Z. Eikeland, M. Stingaciu, A.H. Mamakhel, M. Saura-Múzquiz, M. Christensen, Enhancement of magnetic properties through morphology control of SrFe<sub>12</sub>O<sub>19</sub> nanocrystallites, *Sci. Rep.* 8 (2018) 1–9, <https://doi.org/10.1038/s41598-018-25662-8>.
- [13] A. Quesada, G. Delgado, L. Pascual, A.M. Aragón, P. Marín, C. Granados-Miralles, M. Foerster, L. Aballe, J.E. Prieto, J. De La Figuera, J.F. Fernández, P. Prieto, Exchange-spring behavior below the exchange length in hard-soft bilayers in multidomain configurations, *Phys. Rev. B* 98 (2018) 1–7, <https://doi.org/10.1103/PhysRevB.98.214435>.
- [14] F. Kools, Action of a silica additive during sintering of strontium hexaferrite. Part II: phase diagram, (sub) micron secondary phases and grain boundaries, grain growth and grain growth impediment, reaction induced grain growth impediment, *Sci. Sinter.* 17 (1985) 63–80, <https://www.scopus.com/inward/record.uri?eid=2-s2.0-0021940571&partnerID=40&md5=3b28ae87d648113ab232b358f71528a3>.
- [15] F. Kools, Action of silica additive during sintering of strontium hexaferrite. Part I: preparation and examination of sintered materials, the chemical action of silica, grain growth inhibition by precipitate drag, *Sci. Sinter.* 17 (1985) 49–62, <https://www.scopus.com/inward/record.uri?eid=2-s2.0-0021946690&partnerID=40&md5=f798aed9c651e47f2002163307505253>.
- [16] F.X.N.M. Kools, Science and Technology of Ferrite Magnets: Modelling of Coercivity and Grain Growth Inhibition, Technische Universiteit Eindhoven, 2003, <https://doi.org/10.6100/IR562293>.
- [17] J. Töpfer, S. Schwarzer, S. Senz, D. Hesse, Influence of SiO<sub>2</sub> and CaO additions on the microstructure and magnetic properties of sintered Sr-hexaferrite, PhD Thesis, J. Eur. Ceram. Soc. (2005), <https://doi.org/10.1016/j.jeurceramsoc.2004.06.003>.
- [18] S. Hussain, A. Maqsood, Influence of sintering time on structural, magnetic and electrical properties of Si-Ca added Sr-hexa ferrites, *J. Magn. Magn. Mater.* 316 (1) (2007), <https://doi.org/10.1016/j.jmmm.2007.03.206>.
- [19] J. Bae Lee, H. Jin Kim, J. Luznik, A. Jelen, D. Pajic, M. Wencka, Z. Jaglicic, A. Meden, J. Dolinsek, Synthesis and magnetic properties of Hematite particles in a “Nanomedusa” morphology, Hindawi Publishing Corporation, *J. Nanomater.* 2014 (2014) 9, <https://doi.org/10.1155/2014/902968>.
- [20] I. Lorite, L. Pérez, J.J. Romero, J.F. Fernandez, Effect of the dry nanodispersion procedure in the magnetic order of the Co<sub>3</sub>O<sub>4</sub> surface, *Ceram. Int.* 39 (2013) 4377–4381, <https://doi.org/10.1016/j.ceramint.2012.11.025>.
- [21] V. Lopez-Dominguez, A. Quesada, J.C. Guzmán-Mínguez, L. Moreno, M. Lere, J. Spottorno, F. Giacomone, J.F. Fernández, A. Hernando, M.A. García, A simple vibrating sample magnetometer for macroscopic samples, *Rev. Sci. Instrum.* 89 (2018), <https://doi.org/10.1063/1.5017708>.
- [22] J.F. Fernández, A.C. Caballero, P. Durán, C. Moure, Improving sintering behaviour of BaTiO<sub>3</sub> by small doping additions, *J. Mater. Sci.* 31 (1996) 975–981, <https://doi.org/10.1007/BF00352898>.
- [23] Q. Wu, Z. Yu, H. Hao, Y. Chu, H. Xie, The effect of pH value on strontium hexaferrites: microstructure and magnetic properties, *J. Mater. Sci. Mater. Electron.* 28 (2017) 12768–12775, <https://doi.org/10.1007/s10854-017-7104-2>.
- [24] K. Cendrowski, X. Chen, B. Zielinska, R.J. Kalenczuk, M.H. Rummeli, B. Büchner, R. Klingeler, E. Borowiak-Palen, Synthesis, characterization, and photocatalytic properties of core/shell mesoporous silica nanospheres supporting nanocrystalline titania, *J. Nanoparticle Res.* 13 (2011) 5899–5908, <https://doi.org/10.1007/s11051-011-0307-1>.
- [25] J. López-Sánchez, A. Serrano, A. Del Campo, M. Abuín, O. Rodríguez De La Fuente, N. Carmona, Sol-gel synthesis and micro-Raman characterization of ε-Fe<sub>2</sub>O<sub>3</sub> micro- and nanoparticles, *Chem. Mater.* 28 (2016) 511–518, <https://doi.org/10.1021/acs.chemmater.5b03566>.
- [26] J. López-Sánchez, A. Serrano, A. Del Campo, M. Abuín, E. Salas-Colera, A. Muñoz-Noval, G.R. Castro, J. De La Figuera, J.F. Marco, P. Marín, N. Carmona, O. Rodríguez De La Fuente, Self-assembly of iron oxide precursor micelles driven by magnetic stirring time in sol-gel coatings, *RSC Adv.* 9 (2019) 17571–17580, <https://doi.org/10.1039/c9ra03283e>.
- [27] A. Quesada, A. Del Campo, J.F. Fernández, Stabilization of cubic phase in dense Eu<sub>2</sub>O<sub>3</sub> ceramics, *Mater. Lett.* 157 (2015), <https://doi.org/10.1016/j.matlet.2015.05.085>.